TECHNICAL ARTICLE

Crystallography of Fe–Mn–Al–Ni Shape Memory Alloys

A. Leineweber[1] · A. Walnsch[1] · P. Fischer[1] · H. Schumann[1]

Abstract The microstructure of the martensite formed in Fe–Mn–Al–Ni alloys of varying composition, consisting of A2 austenite and A1-like martensite, was investigated by means of electron backscatter diffraction (EBSD). While sufficiently structured EBSD patterns clearly revealed a tetragonal distortion of the (twinned) martensite, robust indexing using Hough-transform-based methods were successful only by assuming a cubic symmetry of the martensite. It was shown that predictions made based on the Phenomenological Theory of Martensite Crystallography (PTMC) were well compatible with the experimental data, irrespective of the alloy composition. This includes a (near-)Pitsch orientation relationship and habit planes close to $\{110\}_{A2}$.

Introduction

The martensitic transformations in the majority of Fe-based alloys are strongly non-thermoelastic, making them typically unsuitable for shape memory applications.

Nevertheless, some groups of Fe-based shape memory alloys (SMA) [1–4] are exceptionally thermoelastic and have attracted considerable interest because of their relatively low price, which makes them relevant especially in large-scale applications e.g., in architecture. One group of these Fe-based SMAs are based on the Fe–Mn–Al–Ni system. This group has been introduced in 2011 by investigation of the superelasticity of an $Fe_{43.5}Mn_{34}Al_{15}$-$Ni_{7.5}$ alloy [5–7]. In that group the austenite exhibits a body-centered cubic (bcc) A2 structure, whereas the martensite is generally described as a face-centered cubic (fcc) A1 structure, where, however, also tetragonally distorted A1 and polytypic structures have been reported.

The present paper reviews the contradictory crystal structure information shown for Fe–Mn–Al–Ni SMAs. This is done in view of analyzing the martensite crystallography and applying the Phenomenological Theory of Martensite Crystallography (PTMC) [8]. These predictions are compared with results of electron backscatter diffraction (EBSD) analysis. For that purpose, EBSD patterns were evaluated in view of the PTMC predictions from a series of Fe–Mn–Al–Ni alloys with varying composition, containing an austenite matrix with thermally induced martensite.

Methods

PTMC Calculations

The crystallographic characteristics of the austenite (A2) to martensite (cubic or tetragonally distorted A1) transformation are evaluated using the PTMC [9–12]. Corresponding calculations which predict habit planes and orientation relationships were performed using the PTCLab

✉ A. Leineweber
andreas.leineweber@iww.tu-freiberg.de

[1] Institute of Materials Science, TU Bergakademie Freiberg, 09599 Freiberg, Germany

software [13] and, in parallel, an equivalent MATLAB code [14]. A Bain-like lattice correspondence is adopted with a correspondence matrix **C** [15] relating the basis vectors of the body-centered cubic (A2) unit cell of the austenite with those of the martensite in a face-centered cubic or a face-centered tetragonal A1 structure:

$$\begin{pmatrix} \mathbf{a}_{A1} \\ \mathbf{b}_{A1} \\ \mathbf{c}_{A1} \end{pmatrix} = \mathbf{C}^{-T} \begin{pmatrix} \mathbf{a}_{A2} \\ \mathbf{b}_{A2} \\ \mathbf{c}_{A2} \end{pmatrix} = \begin{pmatrix} 1 & -1 & 0 \\ 1 & 1 & 0 \\ 0 & 0 & 1 \end{pmatrix} \begin{pmatrix} \mathbf{a}_{A2} \\ \mathbf{b}_{A2} \\ \mathbf{c}_{A2} \end{pmatrix}$$

The Bain strain matrix is calculated as usual [10] from the actually adopted lattice parameters, where in the tetragonal case the $\mathbf{c}_{A1}$ vector corresponds to the fourfold axis. A lattice invariant strain corresponding to a shear $\langle \bar{1}01 \rangle \{ \bar{1}0\bar{1} \}_{A2}$ in the A2 austenite was considered. The magnitude of the lattice invariant strain and the lattice rotation of the martensite with respect to the austenite were determined under the condition to obtain an invariant plane strain providing the final information about the orientation relationship (OR) and the habit plane.

Alloy Preparation

Five Fe–Mn–Al–Ni alloys of the nominal compositions $Fe_{45}Mn_{34}Al_{14}Ni_7$, $Fe_{42}Mn_{36}Al_{14}Ni_8$, $Fe_{40}Mn_{39}Al_{15}Ni_6$, $Fe_{30}Mn_{48}Al_{17}Ni_5$, and $Fe_{21}Mn_{58}Al_{17}Ni_4$ (the stoichiometric indices basically correspond to molar fractions in %) were prepared by arc melting of pure metal mixtures (Al: 99.9995 wt%, Fe: 99.99 wt%, Mn: 99.95 wt%, Ni: 99.995 wt%, Alfa Aesar/Thermo Fisher GmbH, Germany). The pure metals were placed in a water-cooled copper mold inside an arc-melting furnace (Edmund Buehler GmbH, Germany) under an inert argon atmosphere at a pressure of 800 mbar. In order to achieve a sufficient homogeneity of the resulting specimen, the alloys were turned over and re-melted at least three times. Subsequently, a heat treatment was performed for all samples in a horizontal tube furnace (Linn Elektro Therm GmbH, Germany) at 1200 °C for 24 h, followed by ice water quenching. To prevent oxidation during the heat treatment, the samples were sealed in fused silica ampoules under a controlled argon pressure of 200 mbar. Finally, to facilitate the following EBSD analysis, a metallographic preparation was performed on embedded samples, with a final vibrational polishing step.

EBSD Analysis

Scanning electron microscopy (SEM) investigations were performed on the prepared cross-sections of the specimen in a JSM-7800 F (JEOL Ltd., Japan), which was operating at 30 kV. For the following EBSD investigations, the EBSD camera EDAX Hikari Super Elite was used. The presented EBSD patterns and EBSD maps were acquired using the EDAX TEAM software. In order to perform a sufficiently good background subtraction, which tends to be challenging for coarse-grained materials, $Fe_{40}Ni_{40}B_{20}$ metallic glass was additionally embedded and polished during sample preparation. Due to the similar electron density, compared to the investigated material, the static EBSD background generated from the metallic glass can be used for a subsequent EBSD investigation [16]. For the purpose of identification of grain (and phase) boundary, grains were identified to consist of a minimum of 20 neighbored pixels, where separate grains were assigned in case of a misorientation of 10°. For more details on the EBSD analysis, see [16].

Crystallographic Characteristics

Assessment of Existing Crystallographic Information[1]

In the first work of the development of Fe–Mn–Al–Ni SMAs, it was shown that by balancing the effects of the alloying elements Mn and Al, the thermodynamics of the α and γ phases in Fe–Mn–Al alloys could be adjusted to transform a non-thermoelastic martensitic A2 ("bcc") to A1 ("fcc") transition, which was investigated in some detail on an $Fe_{49}Mn_{36}Al_{15}$ [17] alloy into a thermoelastic one. It was pointed out that, in particular, the magnetic contribution to the overall energetics of these two phases was crucial to adjust the thermodynamic properties of the α and γ phases to achieve the aforementioned type of martensitic transition. The martensite structure was shown to be finely twinned fcc by methods of selected area electron diffraction (SAED). Powder X-ray diffraction (PXRD) data of the alloys (Table 1) confirmed these structures and gave lattice parameter values indicating a volume change of only − 0.4% upon the martensitic transformation.

The actual $Fe_{43.5}Mn_{34}Al_{15}Ni_{7.5}$ alloy introduced in Ref. [5] showed PXRD data with extracted cubic lattice parameters (also included in Table 1), with the martensite peaks showing, however, a considerable broadening. That broadening might also imply a limited precision of the value determined for the martensite. Hence, one probably should not overinterpret a predicted volume change of + 1.1% upon martensite formation.

In the same work [5], SAED patterns of the martensite were presented revealing an eightfold polytypic structure

---

1 Details of the discussed crystal structures are provided in the supplementary material, where also CIF files for the different crystal structures are available.

Table 1 Crystallographic data for phases relevant for Fe–Mn–Al–Ni shape memory alloys

| Year	Alloy	Structure	References
2009	$Fe_{49}Mn_{36}Al_{15}$	A2 austenite: a_{A2} = 2.912 Å (X-ray diffraction)	[17]
2009	$Fe_{49}Mn_{36}Al_{15}$	A1 martensite (2 M) a_{A1} = 3.664 Å (X-ray diffraction)	[17]
2011	$Fe_{43.5}Mn_{34}Al_{15}Ni_{7.5}$	A2 austenite: a_{A2} = 2.903 Å (X-ray diffraction)	[5]
2011	$Fe_{43.5}Mn_{34}Al_{15}Ni_{7.5}$	A1 martensite (2 M) a_{A1} = 3.672 Å (X-ray diffraction)	[5]
2012	$Fe_{43.5}Mn_{34}Al_{15}Ni_{7.5}$	8M martensite, from high-resolution transmission electron microscopy, no further details	[27]
2013	$Fe_{43.5}Mn_{34}Al_{15}Ni_{7.5}$	8M martensite due to [27], lattice parameters a_{8M} = 4.497 Å, b_{8M} = 2.597 Å, c_{8M} = 17.025 Å, β_{8M} = 95°, evidently lattice parameters derived from a_{A1} = 3.672 Å	[18]
2017	$Fe_{43.5}Mn_{34}Al_{15}Ni_{7.5}$	A1 martensite identified by EBSD	[32]
2021	$Fe_{21}Mn_{58}Al_{17}Ni_4$	Tetragonally distorted A1 martensite, $c/a \approx 0.96$	[16]
2021	$Fe_{44}Mn_{37}Al_{14}Ni_5$	Tetragonally distorted A1 martensite, $c/a \approx 0.97$, $L1_0$ like precipitates	[20]
2021	$Fe_{21}Mn_{58}Al_{15}Ni_4$	Tetragonally distorted A1 martensite with $D0_{22}$ superstructure, $c/a \approx 0.97$, selected area electron diffraction	[20]

for the martensite. Based on high-resolution electron microscopy, in this polytype, which was identified have "on average" an $5\overline{3}$ stacking sequence using a Zhdanov type nomenclature, where, however, an irregularity of the stacking was emphasized [5]. Monoclinic lattice parameters referring to this polytype were given in [18] (included in Table 1). Their values imply that they were derived from an ideal close-packed structure having the interatomic distance expected for an A1 structure with a cubic lattice parameter of a_{A1} = 3.672 Å from Ref. [5]. Thereby, it holds for the listed values a_{8M} = $6^{1/2}/2$ a_{A1}, b_{8M} = $2^{1/2}/2$ a_{A1}, c_{8M} = $86^{1/2}/2$ a_{A1}, and $\cos\beta_{8M}$ = $-129^{-1/2}$. It is, however, to be noted that the structure corresponding to such an ideal 8M polytype is compatible with the hexagonal-rhombohedral symmetry, with $a_R = b_R = 2^{1/2}/2$ a_{A1} and $b_{8M} = 8 \times 3^{1/2} a_{A1}$.

SAED data shown in some later works, however, appeared to lack of the features of 8M polytypes and were interpretable in terms of a twinned A1 structure [19, 20], while in [19, 21] also an evidence for long-period polytypism is visible in *some* of the shown patterns. Hence, it appears that the actual structure of the martensite may depend on details of the prior state of the austenite and formation conditions of the martensite.

The diverging reports on the martensite structure might also be related with the state of precipitation in the austenite, which have been made responsible for the pseudoelasticity in $Fe_{43.5}Mn_{34}Al_{15}Ni_{7.5}$ in comparison to the non-thermoelastic alloy $Fe_{49}Mn_{36}Al_{15}$ [5]. These precipitates were characterized to be of the B2 structure inside an A2 austenite in view of their superstructure reflections in SAED patterns [5]. It was shown that the state of aging at low temperatures (around 473 K) strongly influences the pseudoelastic properties of $Fe_{43.5}Mn_{34}Al_{15}Ni_{7.5}$ [22–25] and also the martensite start temperature [23, 26].

In association with the formation of the 8M martensite, the B2 precipitates were reported to experience shear of about 5° [27], where the precipitates appear to retain coherence with the martensite. Contrasting this, SAED patterns on twinned A1 martensite showed superstructure reflections at the positions expected for an $L1_0$ structure [20]. This suggests that the $L1_0$ structure is a product of the same Bain strain applied on the B2 precipitates, which brings about the A2 → A1 transformation for the matrix (note that the Bogers–Burgers path emphasized in [28] basically leads to the same result). As shown in Fig. 1, Bain strain applied in each of the three $\langle 100\rangle_{B2}$ directions yields in an $L1_0$ superstructure of A1, whereas starting from an $L1_0$ structure, a Bain strain leads back to B2 only along one of three possible directions, whereas the other two directions lead to a different and likely high-energy superstructure. This high-energy superstructure can be referred by its Pearson symbol to $oC4$, which tends to efficiently block the "wrong" Bain path. This characteristic transformation pattern for the precipitates has been connected with the reversibility of the martensitic transformation of the $Fe_{43.5}Mn_{34}Al_{15}Ni_{7.5}$ material as a whole [20].

It is known for various reasons that martensites having experienced the Bain strain may be found to be tetragonal [29]. Hence, it is not surprising that more detailed analysis of the SAED patterns of A1-type martensites showing additionally $L1_0$ superstructure reflections from the precipitates revealed tetragonality with $c_{A1}/a_{A1} < 1$ (which is frequently described as a "face-centered tetragonal (fct)" structure) [20]. Upon assessing the diffraction effects due to the coherency of A1/$L1_0$ structures, it has to be kept in mind that such coherent, structurally very similar structures simultaneously contribute to the diffraction patterns and thus to the fundamental reflections. Hence, one may argue that the tetragonal symmetry of the $L1_0$ ordered structure
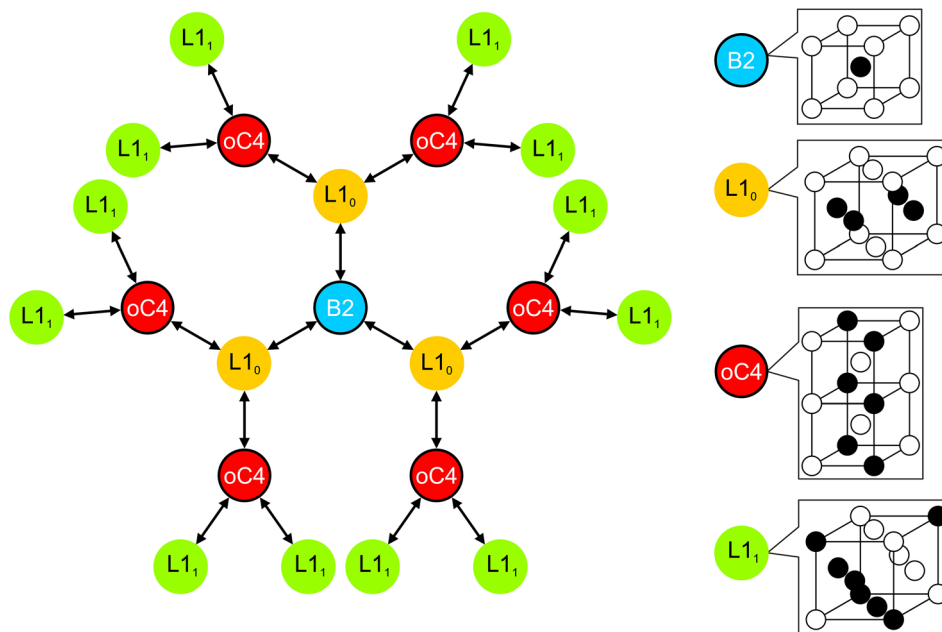
Fig. 1 Bain paths of the A2 and A1 superstructures with two atoms per primitive unit cell (illustrated on the right) relevant for the precipitates: Part of a(n infinite) phase transformation graph in the sense of [31], extending a version shown in Ref. [20]. Each double arrow shows a Bain-type transition path between an A2 and A1 superstructure state. Starting from each structure three Bain paths are possible. Note that starting from an $L1_1$ structure all three arrows go to a different oC4 state. Moreover, note that no transformation path was drawn closed. Note that the structure illustrations on the right do not depict true unit cells in the case of oC4 and $L1_1$. More details on the structures can be found in the supplementary material

appears to justify the observed tetragonality. This view can be refined to some degree by revealing that the energy landscape of NiAl B2 intermetallic, which has a composition close to that of the precipitates, implies that an $L1_0$ structure is actually not a local minimum in energy space under hydrostatic pressure, regardless of the actual degree of distortion. Instead, such $L1_0$ is elastically unstable [26, 30]. Hence the $L1_0$ precipitates should not be regarded as an own stable phase, but severely, non-hydrostatically strained B2. It has been shown that the low martensite start temperatures encountered for Fe–Mn–Al–Ni alloys close to the $Fe_{43.5}Mn_{34}Al_{15}Ni_{7.5}$ composition are caused by a very large energy contribution due to the distorted B2 precipitates [26]. Consequently, the tetragonality of the martensite is a result of the mechanical equilibrium between the A1 matrix and the B2 precipitates that are forcedly strained by the A1 matrix and transformed into that structure due to the chemical driving force. The A1 matrix, in principle, could be fully cubic in the absence of the distortion due to the precipitates, see e.g., [17].

The investigations on the martensite's structure in $Fe_{43.5}Mn_{34}Al_{15}Ni_{7.5}$ were supplemented by investigations on Mn-rich Fe–Mn–Al–Ni alloys [16]. EBSD analysis revealed a finely twinned tetragonal martensite, whereas SAED patterns revealed the presence of a tetragonal (twinned) $D0_{22}$ fcc superstructure, which is related via the Bain strain to a $D0_3$ (or Heusler) bcc superstructure. It was

concluded from the (as compared to $Fe_{43.5}Mn_{34}Al_{15}Ni_{7.5}$ martensite) very clear Kikuchi bands in the EBSD patterns from the bright field electron microscopy images and from the very pronounced $D0_{22}$ superstructure reflections that this $D0_3$ superstructure is the actual structure of the parent austenite which is free from precipitates.

PTMC Considerations

Predictions on the crystallography of the martensite formation in $Fe_{43.5}Mn_{34}Al_{15}Ni_{7.5}$ have been made previously based on assumption of the transition of A2 austenite to 8M martensite [18]. The most important outcomes have been listed in Table 2.

For our own calculation purpose, we assume a Bain-like stretch in $[001]_{A2}$ direction in accordance with three sets of lattice parameters referred to as the cases (i), (ii) and (iii) (see Table 2). The habit planes and the macroscopic shear directions listed in Table 2 pertain to this direction of Bain stretch in combination with a lattice invariant shear on $[\bar{1}01]_{A2}(\bar{1}0\bar{1})_{A2}$ to be realized by twinning.

The three types of calculations were performed in case (i) for the type of cubic lattice parameters as reported in [5], in case (ii) for a modified cubic lattice parameters of the martensite leading to a zero volume change upon martensitic transformation, which is ideally expected for a thermoelastic transformation [33], and in case (iii) for a

Table 2 Results of the PTMC calculation according to the cases (i)–(iii) differing by the crystallographic parameters of the martensite

Case	Austenite	Martensite	Habit plane in austenite coordinates	Martensite habit planes	Macroscopic shear direction in austenite coordinates	magnitude of shape strain
(i)	A2 a_{A2} = 2.903 Å	A1 a_{A1} = 3.672 Å	(.16779, ± .64555, − .74506)	(− .46543, .56742, − .67927)	[− .15007, ± .73034,.6664]	.22795
				(.56742, − .46543, − .67927)		
(ii)	A2 a_{A2} = 2.903 Å	A1 a_{A1} = 3.658 Å = $2^{1/3} a_{A2}$	(.17893, ± .66459, − .72547)	(− .47046, .58476, − .66085)	[− .15942, ± .74615, .64640]	.23165
				(.58476, − .47046, − .66085)		
(iii)[a]	A2 a_{A2} = 2.903 Å	tetragonally distorted A1 a_{A1} = 3.720 Å, c_{A1} = 3.571 Å	(.14646, ± .65174, − .74417)	(− .47744, .56931, − .66928)	[− .13270, ± .72644, .67430]	.20043
				(.56931, − .47744, − .66928)		
[18][b]	A2 a_{A2} = 2.903 Å	a_{8M} = 4.497 Å, b_{8M} = 2.597 Å, c_{8M} = 17.025 Å, β_{8M} = 95°	(.1678, ± .6689, .7451)	–	[− .15901, ± .7303, .6664]	.2369

The solutions listed result from a $\left[\bar{1}01\right]_{A2}\left(\bar{1}0\bar{1}\right)_{A2}$ lattice invariant shear generating twinning as well as a lattice correspondence as given in "PTMC Calculations" section

[a]Implying a volume increase by 1% like in (i) and imposing an axial ratio of 0.96

[b]After adjustment of the plane and directional indices to agree with those of (i)–(iii)

tetragonally distorted ("face-centered tetragonal") fcc structure with c_{A1}/a_{A1} = 0.96 and a volume increase of 1%. The solutions listed in Table 2 for these cases are those two degenerate solutions corresponding to the smallest amount of total strain, while two (also degenerate) solutions corresponding to a larger value of total strain are neglected.

Evidently, the results obtained with the A2 and A1 lattice parameters from [5] used in calculation (i) agree quite precisely with those obtained in Ref. [18] assuming an 8M-like martensite with lattice parameters calculated with the cubic lattice parameters as assessed in [5] (see "Assessment Of Existing Crystallographic Information" section and Table 1). This is understandable if one considers that the twinning assumed as lattice invariant shear in the calculation (i) is partially incorporated microscopically into the 8M structure in terms of a nanotwinning in [5, 27].

The habit planes predicted for cases (i)–(iii) differ at maximum by about 2°, and the correspondingly predicted orientations for the martensite with respect to the austenite differ by about half that value, as depicted in Fig. 2. In particular, the spread of the habit planes for the different cases (i)–(iii) is beyond the typical accuracy of habit plane

determination using trace analysis by EBSD. Hence, these variations are ignored in the present work.

As shown, however, in Fig. 2, the predicted orientation relationships closely correspond to a Pitsch OR [34] ideally expressed as $\{100\}_{A1/fct}||\{1\bar{1}0\}_{A2}$ and $\langle01\bar{1}\rangle_{A1/fct}||\langle11\bar{1}\rangle_{A2}$ when it refers to the variants listed in Table 2.

Results and Discussion

Evaluation of Individual Kikuchi Patterns

Figure 3 depicts EBSD patterns of the austenite and martensite in three of the investigated Fe–Mn–Al–Ni alloys. The patterns of the most Mn-rich $Fe_{21}Mn_{58}Al_{17}Ni_4$ composition have been analyzed in detail in Ref. [16]. This revealed the tetragonality of the martensite, which was later confirmed by SAED [20] and attributed to a $D0_{22}$ superstructure likely inherited from $D0_3$ ordering in the austenite (see also "Assessment of Existing Crystallographic Information" section). Moreover, the martensite was twinned on $(111)_{A1/fct}$ leading to presence of Kikuchi
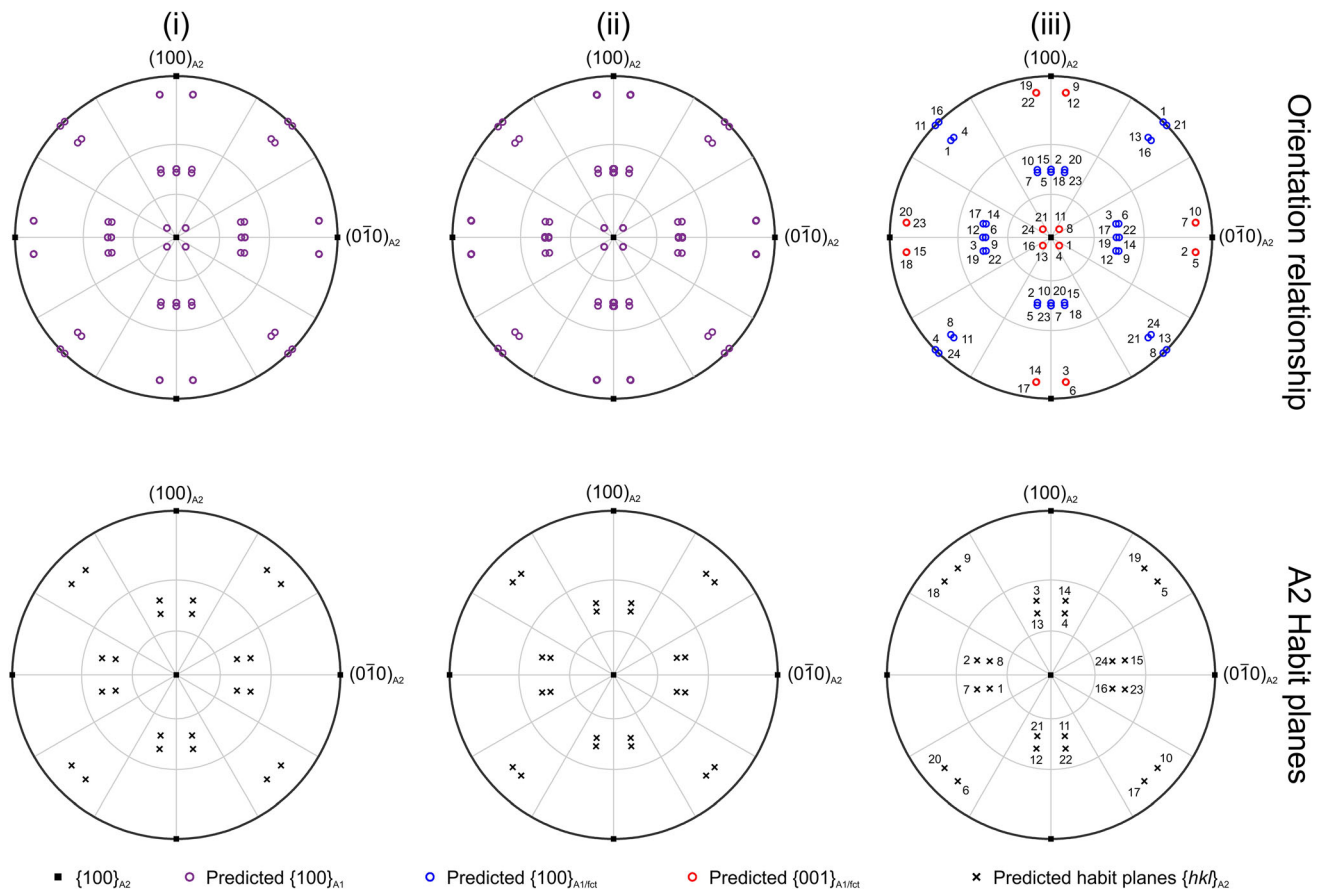
Fig. 2 Predicted orientation relationships (top) and the different habit planes (bottom) for the 24 variants for cases (i)–(iii) considered in Table 2, as plotted in a stereographic projection of the A2 austenitic matrix in cube orientation. In the case of the tetragonal martensite, the $\{001\}_{A1/fct}$ poles correspond to those assembled around the $\{100\}_{A2}$ poles. Note also the habit planes form characteristic quadruples around the $\{110\}_{A2}$ poles. The variant number shown in (iii) are analogous for (i) and (ii) and refer to the Tables S3-S5 given as supplementary material

bands due to a majority and minority component in each variant, as also compatible with the PTMC considerations (see "PTMC Considerations" section). Quite prominently visible is the $(111)_{A1/fct}$ band corresponding to the twinning plane, as also shown in Fig. 3 bottom right. This is one of the polytype invariant bands discussed in Ref. [16], and it is approximately parallel to a $(101)_{A2}$ band (Fig. 3 top right) due to the Bain distortion and the resulting *approximate* Bain-like OR predicted by the PTMC considerations (see Fig. 2 but also what follows in "Results From Cubic Indexing of Martensite" and "Attempts of Tetragonal Indexing" sections). The tetragonality is clearly visible in the differently developed $\left[11\overline{2}\right]_{A1/fct}$ and $\left[\overline{1}2\overline{1}\right]_{A1/fct}$ poles (with the third index referring to the tetragonal axis) visible in Fig. 3 bottom right.

As already mentioned in Ref. [16], the more Fe-rich alloys yield much more blurry EBSD patterns for the martensite, whereas the austenite patterns remain well pronounced with clear band edges (see Fig. 3 left and middle). This general blurriness makes the $(111)_{A1/fct}$ band

more prominent as visible in the bottom parts of Fig. 3 left and middle. The $\left[01\overline{1}\right]_{A1/fct}$ pole in Fig. 3 bottom middle still shows clear deviations from the appearance as expected for cubic symmetry like in the $\left[01\overline{1}\right]_{A1/fct}$ pole in Fig. 3 top left, confirming again the tetragonal distortion. We refrain, however, from stating the same for the most Fe-rich alloy $Fe_{45}Mn_{34}Al_{14}Ni_7$ based on the blurry martensite pattern for the most Fe-rich alloy, although SAED investigations indicated such tetragonality [20].

Results from Cubic Indexing of Martensite

Upon comparing the calculated pole positions of a tetragonally distorted A1 structure with $c/a = 0.96$ with those of a perfectly cubic A1 fcc structure with coinciding $\langle 100\rangle$, $\langle 010\rangle$, and $\langle 001\rangle$ poles, intermediate poles deviate by angles of up to 1° from each other. This maximum deviation of 1° of pole positions might be regarded as an upper bound for the error made upon orientation determination
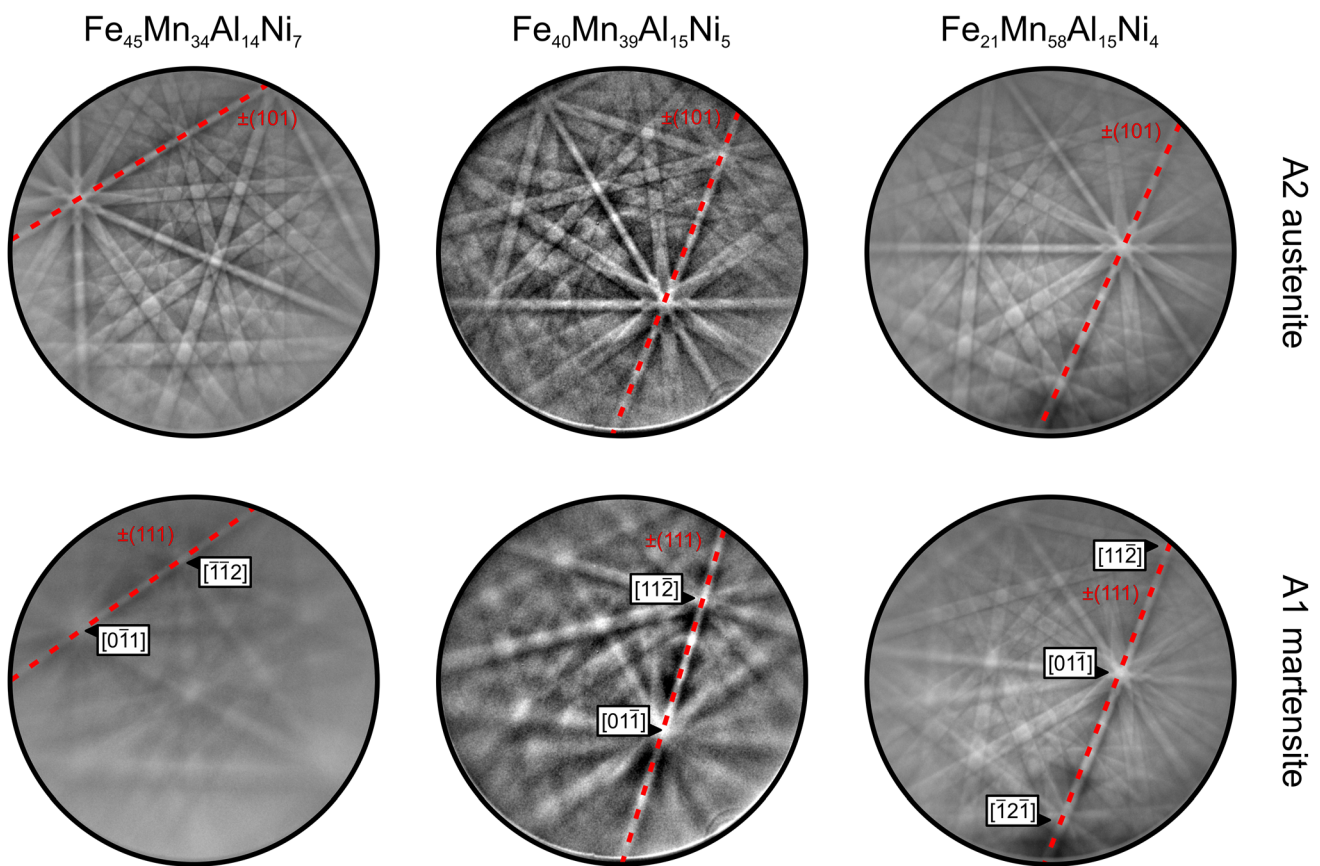
Fig. 3 Typical EBSD patterns of the A2 austenite and the thermally induced twinned A1 martensite taken from the cross-sectionally polished surface of the indicated Fe–Mn–Al–Ni alloys. The martensite patterns were chosen such that the prominent equatorial band $\pm (111)_{A1/fct}$ corresponding to the twinning plane of majority and minority orientation of the martensite is visible. Some poles on this band have been indicated

choosing a potentially inappropriate cubic model for indexing. Correspondingly evaluated data are presented in the following.

Figure 4 depicts EBSD-based maps representing the orientation of the austenite and martensite for the considered alloys. It follows an analysis of the data from the
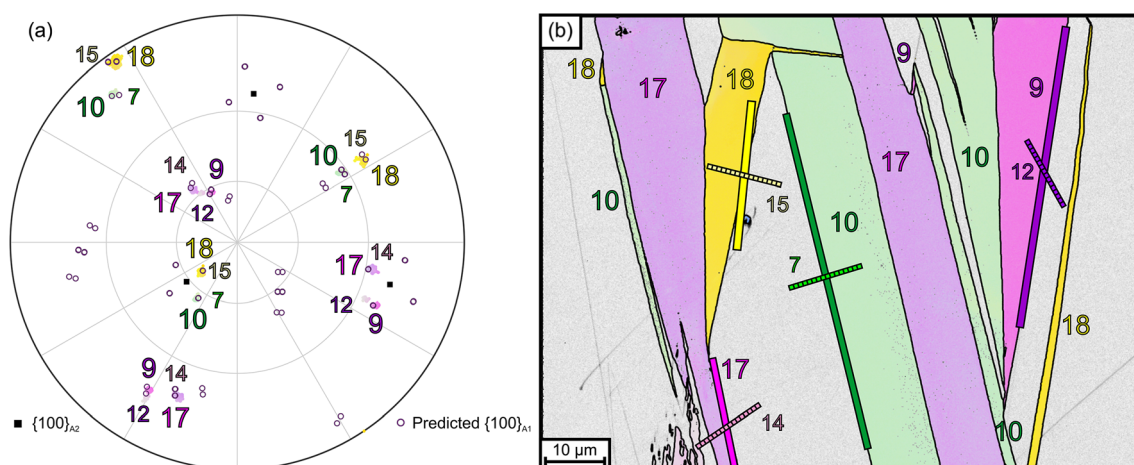
$Fe_{45}Mn_{34}Al_{14}Ni_7$ alloy (Fig. 4 on the far left) in view of the PTMC predictions for case (i) (see Fig. 2 and Table 2). Analysis of the data from the other alloys gives similar results.

Figure 5a shows a stereographic projection determined from the EBSD data from the $Fe_{45}Mn_{34}Al_{14}Ni_7$ alloy. In
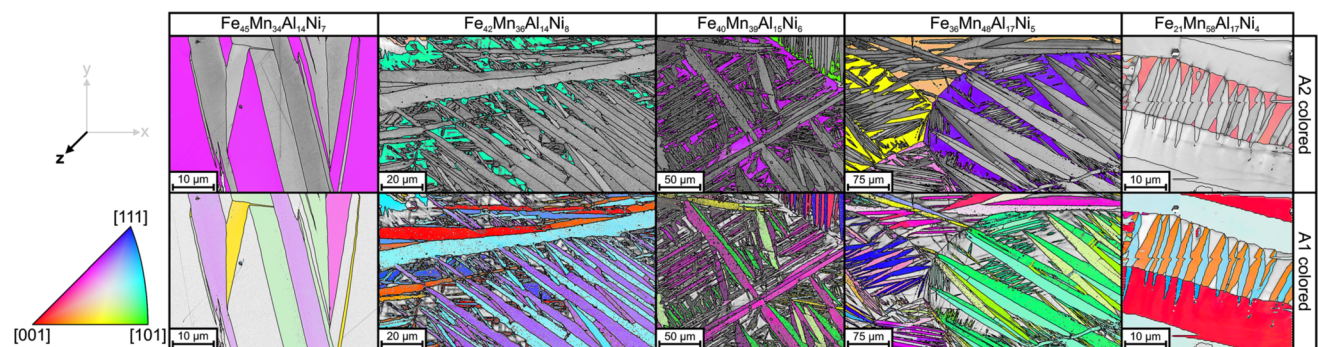
Fig. 4 Results of EBSD measurements from the cross-sectionally polished surface of dual-phase austenite + martensite alloys of the compositions indicated. The maps depict image quality of the uncolored phase in grayscale and IPF color for the indicated phase, applying a cubic indexing for both phases as indicated by the color key. The coloring of the A2 parent austenite reveals the presence of a single or of only few grains in all cases. Grain (variant) and phase boundaries are indicated by black lines

Fig. 5 Test of the results of the PTMC predictions according to case (i) given in Table 2 on the EBSD data from $Fe_{45}Mn_{34}Al_{14}Ni_7$ alloy, as already depicted in Fig. 4 far left. **a** Pole figure depicting the measured average austenite grain orientation as $\{100\}_{A2}$ poles and the $\{100\}_{A1}$ poles predicted by the PTMC for all variants. The observed poles of the A1 martensite are shown with IPF color used for the martensite in Fig. 4 far left bottom, reproduced in **b** with potential variant numbers. In **b** the traces of habit planes predicted using PTMC in view of the potential variants implied by the martensite orientations have been added by colored lines. This allows unequivocal assignment of the variants highlighted by the large numbers, whereas the small numbers are due to the variants compatible with the orientation, but incompatible with the habit planes (Color figure online)

this stereographic projection, the $\{100\}_{A2}$ poles of the average matrix orientation have been indicated together with the predicted positions of the $\{100\}_{A1}$ martensite poles. The colored regions correspond to the $\{100\}_{A1}$ martensite poles according to the observed orientations in the inverse pole figure (IPF) colors as shown in Fig. 4, bottom on the far left. As already evident from Fig. 2, 12 pairs of the altogether 24 variants are predicted to have virtually the same orientation. The habit planes of these two variants can, however, be calculated, respectively, and assume quite distinct orientations in space, as visible from the distribution of variant numbers given in the bottom of Fig. 2.

For the variant numbers resulting from adopting a specific orientation of the parent austenite A2 grain, habit planes have been calculated and their traces have been included in Fig. 5b. In every case, one of two traces corresponding to one of two variants compatible with the orientation data shows much better agreement with the observed habit plane trace, allowing unequivocal identification of the variant. The numbers of the confirmed variants have been added as large numbers in Fig. 5, whereas those of the unconfirmed variants are indicated with smaller numbers.

Accordingly, the predictions from PTMC with respect to OR and with respect to habit plane have been confirmed. As it concerns the OR, a Pitsch OR between austenite and martensite was indeed reported previously based on an EBSD study apparently using fcc/A1 indexing for the martensite [32]. In that work, however, this OR was related with the Bogers–Burgers path of the transformation

without making a connection to the martensite crystallography. In another work, the same group has shown [35] that the traces of the habit planes of the martensite are compatible with the PTMC prediction from [18]. In the present work, it was demonstrated that basically the same habit plane can result, if an A1 structure for the martensite is adopted, only then allowing a relation with the Pitsch OR.

It may be noted finally that the four martensite variants encountered in the EBSD map of the $Fe_{45}Mn_{34}Al_{14}Ni_7$ alloy belong to two different Bain groups, as visible from the distribution of the observed $\{100\}_{A1}$ poles around the $\{100\}_{A2}$ poles. Moreover, all variants have a habit plane close to one single $\{110\}_{A2}$ pole, as it can be seen from inspecting the variant numbers in the bottom part of Fig. 2. Hence, the four variants assemble according to diamond morphology previously observed in other SMAs with A2/B2-type austenite [36, 37] and discussed to be favorable in view of accommodation of the transformation strains of different variants, also in the course of reversible domain switching in the martensitic state [33].

As indicated above, the PTMC predictions due to case (i) are also well fulfilled for the EBSD data for the other investigated alloys. Likewise, the diamond morphology variant combinations observed seem to occur, too.

Attempts of Tetragonal Indexing

Figure 6 depicts the results of EBSD measurements on the $Fe_{40}Mn_{39}Al_{15}Ni_6$ alloy beyond that one shown in Fig. 4 middle. While Fig. 6a highlights the remainders of the parent austenite grains, Fig. 6b shows the orientations of
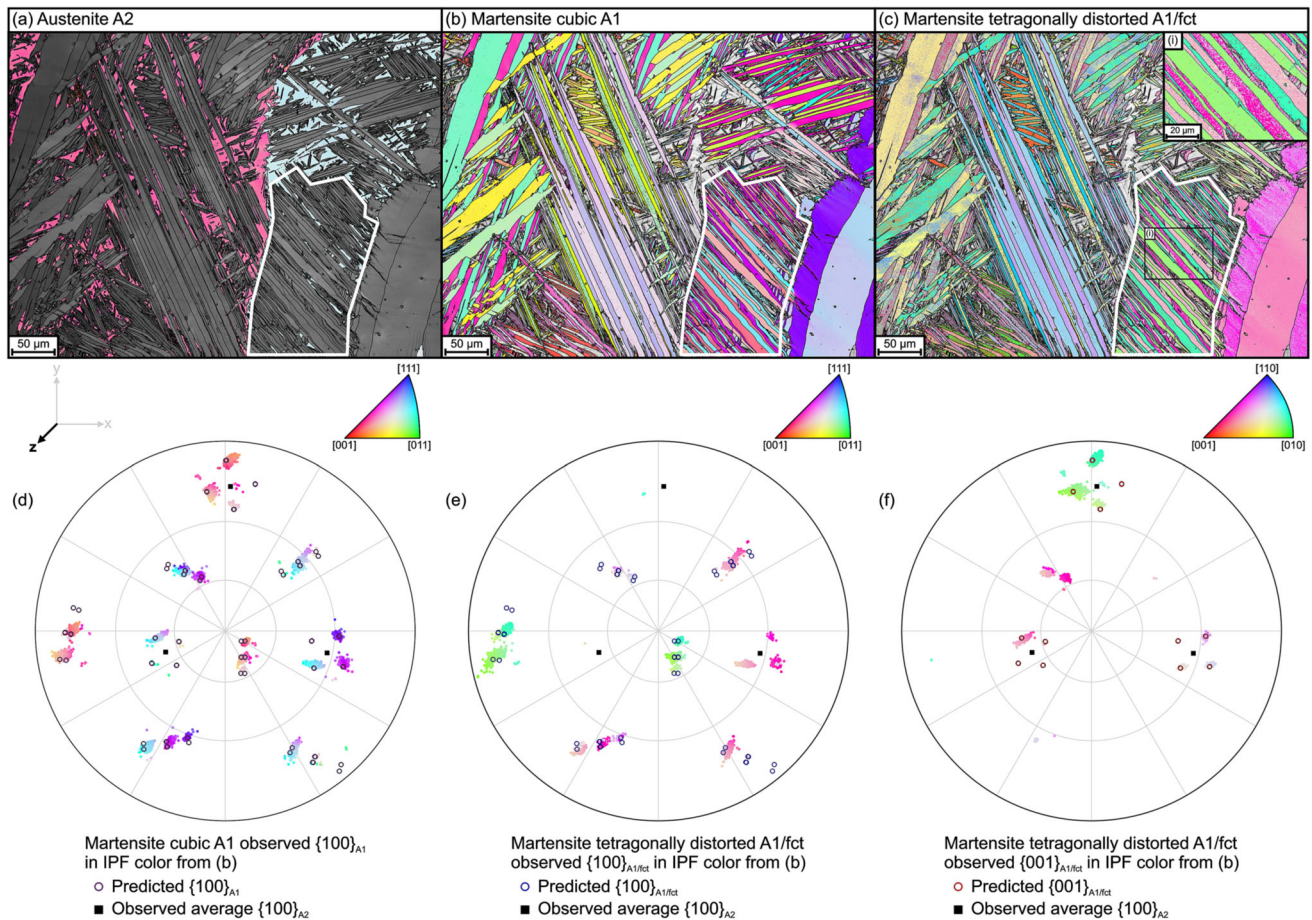
Fig. 6 Results of EBSD measurements from cross-sectionally polished surface of $Fe_{40}Mn_{39}Al_{15}Ni_6$ alloy exhibiting dual-phase austenite + martensite microstructures. **a**–**c** IPF maps depicting the indicated phase in the indicated structure and the other phase in image quality as grayscale. Grain (variant) and phase boundaries are indicated by black lines. The maps reveal **a** the few parent austenite grains, **b** the robust indexing of the martensite with the cubic A1 structure, and **c** indexing using the tetragonally distorted A1 structure.

In **c** many domains show pixels with colors corresponding to up to three different orientations due to the pseudosymmetry, for more details see the magnified inset (i). **d**–**f** Pole figures from the region highlighted by a white solid line in **a**–**c**, showing the average austenite (A2) orientation and the indicated predicted and measured martensite (A1) orientations, revealing incorrect indexing also for some uniformly indexed regions, e.g., those colored in dark pink in **c**

the martensite grains using cubic indexing (case (i)–(ii) from Table 2). Fully compatible with the remarks above, the (near-)Pitsch OR as predicted by PTMC is confirmed.

It was, however, shown in "Evaluation of Individual Kikuchi Patterns" section that the Kikuchi patterns due to the martensite in this $Fe_{40}Mn_{39}Al_{15}Ni_6$ alloy show the features of the tetragonal distortions, as it was evaluated in the case of the martensite in the Mn-rich $Fe_{21}Mn_{58}Al_{17}Ni_4$ alloy in detail in Ref. [16]. In the latter work, convincing indexing also succeeded using pattern-matching methods. In the present work, we restricted ourselves to use the more routinely accessible Hough-transform-based indexing methods. Indexing attempts using a tetragonally distorted structure model corresponding to case (iii) frequently yielded two or three different orientations of the tetragonal c axis of the martensite, which is typically displayed by mutual occurrence of the colors for three different orientations in the IPF

maps as evident in Fig. 6c. Although an axial ratio $c/a = 0.96$ might be sufficiently different from unity to allow tetragonal indexing (see e.g., [38]), in the present case, the presence of the (weaker) bands of the minority twin component in the EBSD patterns likely inhibited always identifying the correct one out of three different orientations of the tetragonal c axis for the majority orientation.

Certain martensite variants, however, appear to be indexed uniformly, e.g., the variants colored pink and green in Fig. 6c within the region marked in Fig. 6a–c. Correctness of the indexing solution can be checked by the proximity of the $\{001\}_{A1/fct}$ poles due to the martensite with the $\{100\}_{A2}$ poles due to the austenite expected from the predicted OR (and the very approximate Bain-like OR). The pole figures reveal, however, that while this proximity occurs for the green-colored variants, many of the pink-indexed points correspond to solutions where the $\{001\}_{A1/}$

fct poles are located in the proximity of $\{110\}_{A2}$ poles (and $\{100\}_{A1/fct}$ close to $\{100\}_{A2}$) as demonstrated in Figure 6e, f is an example how some bias (e.g., uncorrected distortions in the EBSD pattern) might lead the indexing algorithm favoring an incorrect solution. It has not yet been tested whether there is some systematic crystal orientation dependence of the success rate for correct indexing as worked out recently for another tetragonal material with cubic pseudosymmetry [39].

Conclusions

Thermally induced martensite was investigated by electron backscatter diffraction (EBSD) analysis using Hough-transform-based indexing methods in a series of Fe–Mn–Al–Ni alloys derived from the $Fe_{43.5}Mn_{34}Al_{15}Ni_{7.5}$ shape memory alloys. The data were compared with predictions made by the phenomenological theory of martensite crystallography (PTMC). The following conclusions can be drawn from the evaluation of the results:

(i) PTMC predictions assuming an A2 austenite and twinned A1 martensite with different volume and allowance of a small tetragonal distortion in view of the literature evidence gave, with respect to habit planes of the austenite and the macroscopic shear, similar results as previous predictions made using a monoclinic martensite. In view of a face-centered cubic or face-centered tetragonal A1 structure of the martensite, a (near-)Pitsch OR was predicted.

(ii) While alloys with a high Fe content gave very diffuse EBSD patterns, likely due to the B2 precipitates contained in the alloy, alloys with a higher Mn content showed patterns clearly revealing the tetragonal distortion of A1 martensite. However, the assessment of the correct orientation of the tetragonal c axis using the applied Hough-transform-based automatic indexing procedures did not succeed within the present work.

(iii) Indexing using A1 martensite structure, i.e., ignoring possible presence of tetragonal distortion, gave robust indexing of the EBSD patterns. The assessed orientations of the martensite reveal its near Pitsch OR with respect to the A2 austenite, agreeing well with the PTMC predictions. Moreover, the predicted habit planes agree well with habit plane traces visible in the experimental microstructures evident from the EBSD maps. This allows even distinction between martensite variants predicted to have virtually the same OR with respect to the austenite and reveals variant

combinations having one approximate $\{110\}_{A2}$ habit plane in common, also reported for other SMAs.

References

1. Cladera A, Weber B, Leinenbach C, Czaderski C, Shahverdi M, Motavalli M (2014) Iron-based shape memory alloys for civil engineering structures: an overview. Constr Build Mater 63:281–293. https://doi.org/10.1016/j.conbuildmat.2014.04.032
2. Alaneme KK, Okotete EA (2016) Reconciling viability and cost-effective shape memory alloy options—a review of copper and iron based shape memory metallic systems. Eng Sci Technol 19(3):1582–1592. https://doi.org/10.1016/j.jestch.2016.05.010
3. Chowdhury P, Canadinc D, Sehitoglu H (2017) On deformation behavior of Fe-Mn based structural alloys. Mater Sci Eng R 122:1–28. https://doi.org/10.1016/j.mser.2017.09.002
4. La Roca P, Baruj A, Sade M (2017) Shape-memory effect and pseudoelasticity in Fe–Mn-based alloys. Shape Mem Superelast 3(1):37–48. https://doi.org/10.1007/s40830-016-0097-5
5. Omori T, Ando K, Okano M, Xu X, Tanaka Y, Ohnuma I, Kainuma R, Ishida K (2011) Superelastic effect in polycrystalline ferrous alloys. Science 333(6038):68–71. https://doi.org/10.1126/science.1202232
6. Omori T, Kainuma R (2017) Martensitic transformation and superelasticity in Fe–Mn–Al-based shape memory alloys. Shape Mem Superelast 3(4):322–334. https://doi.org/10.1007/s40830-017-0129-9
7. Abuzaid W, Wu Y, Sidharth R, Brenne F, Alkan S, Vollmer M, Krooß P, Niendorf T, Sehitoglu H (2019) FeMnNiAl iron-based shape memory alloy: promises and challenges. Shape Mem

Superelast 5(3):263–277. https://doi.org/10.1007/s40830-019-00230-9

8. Zhang M-X, Kelly PM (2009) Crystallographic features of phase transformations in solids. Prog Mater Sci 54(8):1101–1170. https://doi.org/10.1016/j.pmatsci.2009.06.001

9. Wechsler MS, Lieberman DS, Read TA (1953) On the theory of the formation of martensite. Trans AIME 197:1503–1515

10. Wechsler MS (1959) On the theory of martensitic transformations The generalized lattice invariant shear and the degeneracy of solutions for the cubic to tetragonal transformation. Acta Metall 7(12):793–802. https://doi.org/10.1016/0001-6160(59)90095-1

11. Bowles JS, Mackenzie JK (1954) The crystallography of martensite transformations I. Acta Metall 2(1):129–137. https://doi.org/10.1016/0001-6160(54)90102-9

12. Mackenzie JK, Bowles JS (1954) The crystallography of martensite transformations II. Acta Metall 2(1):138–147. https://doi.org/10.1016/0001-6160(54)90103-0

13. Gu X-F, Furuhara T, Zhang W-Z (2016) PTCLab: free and open-source software for calculating phase transformation crystallography. J Appl Crystallogr 49(3):1099–1106. https://doi.org/10.1107/S1600576716006075

14. Schumann H, Leineweber A (2021) Crystallography of γ'-Fe4N formation on bulk polycrystalline α-Fe substrates. Materialia 101119. https://doi.org/10.1016/j.mtla.2021.101119

15. Christian JW (2002) The theory of transformations in metals and alloys: an advanced textbook in physical metallurgy. International series on materials science and technology, 3rd edn. Elsevier, Burlington

16. Fischer PDB, Martin S, Walnsch A, Thümmler M, Kriegel MJ, Leineweber A (2021) Nanoscale twinning in Fe-Mn-Al-Ni martensite: a backscatter Kikuchi diffraction study. J Appl Crystallogr 54(1):54–61. https://doi.org/10.1107/S1600576720013631

17. Ando K, Omori T, Ohnuma I, Kainuma R, Ishida K (2009) Ferromagnetic to weak-magnetic transition accompanied by bcc to fcc transformation in Fe–Mn–Al alloy. Appl Phys Lett 95(21):212504. https://doi.org/10.1063/1.3266848

18. Omori T, Okano M, Kainuma R (2013) Effect of grain size on superelasticity in Fe-Mn-Al-Ni shape memory alloy wire. APL Mater 1(3):32103. https://doi.org/10.1063/1.4820429

19. Tseng LW, Ma J, Wang SJ, Karaman I, Kaya M, Luo ZP, Chumlyakov YI (2015) Superelastic response of a single crystalline FeMnAlNi shape memory alloy under tension and compression. Acta Mater 89:374–383. https://doi.org/10.1016/j.actamat.2015.01.009

20. Walnsch A, Kriegel MJ, Fischer PDB, Neumann S, Rafaja D, Leineweber A (2021) Nanoscale twinning and superstructures of martensite in the Fe–Mn–Al–Ni system. Materialia 16:101062. https://doi.org/10.1016/j.mtla.2021.101062

21. Tseng LW, Ma J, Vollmer M, Krooß P, Niendorf T, Karaman I (2016) Effect of grain size on the superelastic response of a FeMnAlNi polycrystalline shape memory alloy. Scr Mater 125:68–72. https://doi.org/10.1016/j.scriptamat.2016.07.036

22. Tseng LW, Ma J, Hornbuckle BC, Karaman I, Thompson GB, Luo ZP, Chumlyakov YI (2015) The effect of precipitates on the superelastic response of [100] oriented FeMnAlNi single crystals under compression. Acta Mater 97:234–244. https://doi.org/10.1016/j.actamat.2015.06.061

23. La Roca P, Baruj A, Sobrero CE, Malarría JA, Sade M (2017) Nanoprecipitation effects on phase stability of Fe-Mn-Al-Ni alloys. J Alloys Compd 708:422–427. https://doi.org/10.1016/j.jallcom.2017.02.280

24. Vollmer M, Kriegel MJ, Walnsch A, Klemm V, Leineweber A, Niendorf T (2019) On the microstructural and functional stability of Fe-Mn-Al-Ni at ambient and elevated temperatures. Scr Mater 162:442–446. https://doi.org/10.1016/j.scriptamat.2018.12.008

25. Ozcan H, Ma J, Karaman I, Chumlyakov YI, Santamarta R, Brown J, Noebe RD (2018) Microstructural design considerations in Fe-Mn-Al-Ni shape memory alloy wires: effects of natural aging. Scr Mater 142:153–157. https://doi.org/10.1016/j.scriptamat.2017.07.033

26. Walnsch A, Kriegel MJ, Motylenko M, Korpala G, Prahl U, Leineweber A (2021) Thermodynamics of martensite formation in Fe–Mn–Al–Ni shape memory alloys. Scr Mater 192:26–31. https://doi.org/10.1016/j.scriptamat.2020.10.003

27. Omori T, Nagasako M, Okano M, Endo K, Kainuma R (2012) Microstructure and martensitic transformation in the Fe-Mn-Al-Ni shape memory alloy with B2-type coherent fine particles. Appl Phys Lett 101(23):231907. https://doi.org/10.1063/1.4769375

28. Ojha A, Sehitoglu H (2016) Transformation stress modeling in new FeMnAlNi shape memory alloy. Int J Plast 86:93–111. https://doi.org/10.1016/j.ijplas.2016.08.003

29. Christian JW (1992) Tetragonal martensites in ferrous alloys—a Critique. Mater Trans JIM 33(3):208–214. https://doi.org/10.2320/matertrans1989.33.208

30. Purja Pun GP, Mishin Y (2009) Development of an interatomic potential for the Ni-Al system. Philos Mag 89(34–36):3245–3267. https://doi.org/10.1080/14786430903258184

31. Gao Y, Yu T, Wang Y (2020) Phase transformation graph and transformation pathway engineering for shape memory alloys. Shape Mem Superelast 6(1):115–130. https://doi.org/10.1007/s40830-020-00271-5

32. Vallejos JM, Sobrero CE, Ávalos M, Signorelli JW, Malarría JA (2018) Crystallographic orientation relationships in the $\alpha \rightarrow \gamma'$ martensitic transformation in an Fe-Mn-Al-Ni system. J Appl Crystallogr 51(4):990–997. https://doi.org/10.1107/S1600576718006738

33. Bhattacharya K (2007) Microstructure of martensite: why it forms and how it gives rise to the shape-memory effect. Oxford series on materials modelling, vol 2. Oxford Univ. Press, Oxford

34. Pitsch W (1959) The martensite transformation in thin foils of iron-nitrogen alloys. Philos Mag 4(41):577–584. https://doi.org/10.1080/14786435908238253

35. Vallejos JM, Giordana MF, Sobrero CE, Malarria JA (2020) Excellent pseudoelasticity of Al-rich Fe–33Mn–17Al–6Ni–0.15C (at%) shape memory single crystals obtained without an aging conditioning stage. Scr Mater 179:25–29. https://doi.org/10.1016/j.scriptamat.2019.12.038

36. Schroeder TA, Wayman CM (1977) The formation of martensite and the mechanism of the shape memory effect in single crystals of Cu-Zn alloys. Acta Metall 25(12):1375–1391. https://doi.org/10.1016/0001-6160(77)90069-4

37. Saburi T, Wayman CM (1979) Crystallographic similarities in shape memory martensites. Acta Metall 27(6):979–995. https://doi.org/10.1016/0001-6160(79)90186-X

38. Martin S, Berek H, Aneziris CG, Martin U, Rafaja D (2012) Pitfalls of local and quantitative phase analysis in partially stabilized zirconia. J Appl Crystallogr 45(6):1136–1144. https://doi.org/10.1107/S0021889812038733

39. Pang EL, Schuh CA (2021) Crystal orientation and detector distance effects on resolving pseudosymmetry by electron backscatter diffraction. J Appl Crystallogr 54(2):513–522. https://doi.org/10.1107/S1600576721001229